Supporting Information

Reinhard et al. 10.1073/pnas.1208622110

SI Discussion

Metal Enrichment Database and Filtering Protocols. Through our own analytical efforts and a literature survey, we have assembled a database of molybdenum (Mo) and chromium (Cr) concentrations for over 3,000 samples. Data sources are shown in Table S1. Samples were initially filtered to represent solely fine-grained siliciclastic sediments, using basic petrographic observation and major element thresholds. Samples were required to contain weight percent (wt %) levels of iron (Fe) and aluminum (Al). Samples containing less than 1.0 wt % total organic carbon were also removed.

The information contained within a particular degree of authigenic enrichment of Cr or Mo depends on local depositional redox. Thus, samples were further filtered such that Cr data were only analyzed from anoxic shales, and Mo data were only analyzed from euxinic shales. Anoxic shales were delineated as having $Fe_T/Al > 0.5$ (1) and/or $Fe_{HR}/Fe_T > 0.38$ (2–4), where Fe_{HR} designates "highly reactive" Fe (Fe that is reactive to dissolved H_2S on syngenetic or diagenetic timescales; ref. 5) and Fe_T represents total Fe. Euxinic settings were delineated by combining the above thresholds for anoxia with either $Fe_{PY}/Fe_{HR} > 0.7$ (4, 6) or with elevated values for degree of pyritization (DOP > 0.6; ref. 7), defined as (8)

$$\mathrm{DOP} = \frac{\mathrm{Fe_{PY}}}{\mathrm{Fe_{PY}} + \mathrm{Fe_{HCL}}},$$

where Fe_{HCl} is Fe soluble in a 1-min boiling concentrated HCl leach and Fe_{PY} denotes pyrite Fe. Because elevated DOP has also been shown to require enhanced Fe mobility and transport (1, 7), and because it is an extremely robust analytical measurement, DOP > 0.8 supersedes all other redox filters in the designation of euxinia. In some cases, total sulfur content is used to calculate DOP_T, according to

$$\mathrm{DOP_T} = \frac{\mathrm{Fe_S}}{\mathrm{Fe_S} + \mathrm{Fe_T}},$$

where Fe_S denotes the inferred amount of sulfur-bound Fe assuming that total sulfur represents pyrite sulfur (9). Modern systems (such as the Black Sea and Cariaco Basin) were additionally filtered by site location, for extreme siliciclastic dilution, and the presence of bioturbation, and units with fewer than ten filtered samples were not included in overall statistical calculations.

Our focus here is on the contrast in enrichment records between the mid-Proterozoic and the Phanerozoic. However, as noted in the main text, there appear to be substantial Cr enrichments in late Paleoproterozoic anoxic shales. Recent work has suggested an increase and subsequent decrease in Earth surface oxidation during the Paleoproterozoic (10, 11), and we suggest in the main text that the Cr enrichment pattern is possibly related to this, with the subsequent drawdown of Cr enrichments representing the progressive expansion of anoxic marine environments. Shown in Fig. S1 is the full enrichment record, including Archean and Paleoproterozoic data. The Mo enrichment record in euxinic shales (Fig. S1*B*) is similar to previous work (12), showing minimal enrichment during the Archean and appreciable although muted enrichments (relative to the Phanerozoic) during most of the Proterozoic. The Cr enrichment record shows some very high enrichments during the Archean and Paleoproterozoic (Fig. S1*A*). Some of this trend is almost certainly because Archean upper crust was more mafic in composition, and much of these enrichments could be linked to very Cr-rich source terrains. The Paleoproterozoic enrichments, on the other hand, may well be authigenic enrichments. Future isotopic and petrographic work is required to distinguish between these two models.

Modern Mo Mass Balance. We begin by assuming steady state, wherein a single input flux (F_{in}) is balanced by removal via authigenic burial into three main sedimentary sinks: an oxic sink (F_{ox}), a reducing sediment sink (F_{red}), and a sulfidic sink (F_{sulf}). Our balanced modern Mo budget is shown in Fig. S2 and Table S2, and individual removal terms are discussed below. The weathering flux of Mo on the modern Earth is dominated by the mobilization of Mo from sulfide mineral phases or organics in sedimentary and igneous rocks and transport as dissolved MoO_4^{2-}, and we set as F_{in} a recently obtained modern riverine flux of dissolved MoO_4^{2-} to the ocean (13). This flux is somewhat larger than those conventionally used, but is derived from the most extensive riverine database generated to date, representing 38 rivers across 5 continents and including 11 of 19 large-scale drainage areas. However, regardless of our choice of estimate for the riverine Mo flux, sensitivity analysis (Fig. S3) indicates that our conclusions are weakly sensitive to the assumed value of the input flux over a wide range. We neglect hydrothermal fluxes of Mo to/from the ocean, as these are either poorly established or likely to be quantitatively small (see below).

Oxic settings are defined as those in which Mn is permanently removed from the ocean as an oxide phase (with associated adsorbed Mo). In many oxic deep-sea settings, dissolved O_2 penetrates to the sediment–basalt interface (14, 15) and this Mn (and Mo) will effectively be buried permanently. In other settings, dissimilatory microbial Mn reduction deeper in the sediment column can remobilize Mn (and, presumably, associated Mo). However, when O_2 penetration depths are large (multiple centimeters or more) upward-diffusing Mn will be quantitatively oxidized at a steady-state oxidation front (16–18), effectively removing Mn and Mo from the ocean on a timescale characteristic of tectonic recycling of seafloor sediments (on the order of $\sim 10^8$ y). Morford and Emerson (19) suggest that once O_2 penetration falls below ~1 cm, Mn and Mo will be recycled and released from shallow sediments. We therefore characterize oxic seafloor as being the areal extent of sediments in which O_2 penetration exceeds 1 cm. This is estimated using global diagenetic models (20, 21) to be $\sim 3 \times 10^8$ km^2, or roughly 84% of modern seafloor area. We stress that there are fairly large regions of the seafloor that are essentially Mo neutral (see below), such that the total seafloor area for the entire budget need not sum to 100%. This area is then combined with a burial rate of 2.75×10^{-3} μg·cm^{-2}·y^{-1}, estimated by compiling Mo burial rates in oxic settings (22) and by combining Mn burial rates in oxic pelagic sediments (23) with a characteristic Mo/Mn ratio of 2×10^{-3} (24). The combined sink is shown in Table S2.

Sulfidic settings are defined as environments in which dissolved H_2S accumulates at or above the sediment–water interface. This includes traditional euxinic settings (Black Sea, Cariaco Basin), but is also meant to include small areas of the seafloor below regions of intense upwelling (Peru margin, Namibian shelf), where dissolved H_2S is present at high levels essentially at the sediment–water interface and occasionally breaches into the water column (25, 26). Our sulfidic sink is calculated by combining estimates of seafloor area, authigenic enrichment, and bulk mass accumulation rate (MAR) for modern sulfidic settings (2, 27–39). The globally averaged sulfidic burial calculated

through such an approach will be biased low—given that the modern extent of euxinic seafloor, on an areal basis, is dominated by the Black Sea, and this setting is characterized by low burial rates due to restricted exchange over the Bosporus sill and an evolved Mo reservoir (36). As a result, the global sulfidic burial rates implemented in the model are referenced to a modern globally averaged sulfidic burial rate that neglects the influence of the Black Sea. This is done in an effort to represent the burial capacity of marine settings with unfettered access to the seawater Mo reservoir (12).

The final sink is reducing sediments. This sink represents environments that have been referred to by the rather ambiguous term "suboxic." We follow ref. 12 in designating these environments as those in which dissolved H_2S accumulation is restricted to pore waters, but further point out that reducing sediments in which O_2 penetration is less than ~1 cm and H_2S accumulation occurs more deeply in the sediments do not effectively bury Mo (19). From a mechanistic perspective, these reducing sediment environments are typically associated with relatively low bottom-water O_2, but the effectiveness of Mo sequestration in these settings is most likely a more complex function of Mn flux to sediments (and, thus, bottom-water O_2), sedimentation rate, and labile organic carbon flux to the sediment–water interface. In any case, we use a somewhat moderate burial rate for reducing sediments of 0.27 $\mu g \cdot cm^{-2} \cdot y^{-1}$ (37, 40–43), and use the remaining parameters of the budget to solve for the seafloor area represented by this sink (Table S2). Although we present a revised approach for estimating the global Mo removal fluxes, our result is similar to previous estimates based on consideration of bulk burial rates (12) and isotope mass balance (40).

Modern Cr Mass Balance. As for Mo, we begin by assuming steady state, with a single input flux (F_{in}) balanced by three authigenic burial fluxes: an oxic sink (F_{ox}), a reducing sediment sink (F_{red}), and an anoxic sink (F_{anox}). In our modeling analysis, we take anoxic environments to include those that are euxinic (anoxic and H_2S-rich), ferruginous (anoxic and Fe^{2+}-rich), and NO_3^- buffered (i.e., anoxic but with low concentrations of both H_2S and Fe^{2+}). We note, however, that the latter environments are likely to be spatially and temporally limited, given the relatively low concentration (and thus redox buffering capacity) of NO_3^- in seawater. Potential hydrothermal fluxes to/from the ocean are neglected in our treatment of the modern Cr cycle, as currently available data suggest that these fluxes are quantitatively insignificant (see below). The Cr mass balance is rather poorly constrained—compared with that for Mo. However, we suggest that although our mass balance is likely to be revised as better estimates of fluxes and reservoirs become available, this is very unlikely to change our fundamental conclusions.

Our input flux is calculated following the method of ref. 13. In brief, we compiled a database of dissolved [Cr] values and annual discharge rates for rivers (Table S3), and used this to calculate discharge-weighted dissolved [Cr] values for individual large-scale drainage regions according to the available data. The Cr flux from each large-scale drainage region was then computed by combining the discharge-weighted [Cr] value with the total discharge flux from each region. These regional fluxes were combined and used to estimate a global discharge-weighted dissolved [Cr] value of 14.82 nM. This value was then combined with an estimated global exorheic flux of 3.9×10^4 $km^3 \cdot y^{-1}$ (44), yielding an estimate of the discharge-weighted flux of dissolved Cr to the modern ocean. Although dissolved Cr data are less common than dissolved major ion data for rivers, the large-scale drainage regions in our database account for ~70% of the overall exorheic flux to the oceans. Assuming minimal estuarine removal (45, 46), and combining this estimate with an average seawater concentration of 4 nM (47) and an ocean volume of 1.37×10^{21} L, this yields a residence time for Cr in the modern ocean of ~9,500 y (i.e., over a factor of 9 greater than characteristic timescales of ocean mixing). To our knowledge, estimates of this sort are few, but ours is well in line with previous attempts (e.g., ref. 48). As for Mo, sensitivity analysis (Fig. S3) indicates that our conclusions are not likely to be fundamentally altered unless input fluxes to the ocean become extremely low.

Dissolved Cr(VI) species should become adsorbed onto the surface of metal- and Al-oxide phases (49–51). We therefore expect some nontrivial burial flux of Cr in oxic settings, although we note that sorption to Al-oxide phases decreases sharply when approaching circumneutral pH (52). The Cr content of pelagic red clays, although often elevated above crustal values with respect to Cr/Ti ratios, is rather variable. We use in our budget a relatively low oxic Cr burial rate of 1.0×10^{-3} $\mu g \cdot cm^{-2} \cdot y^{-1}$, of the same order as our much better constrained Mo burial flux. This corresponds to a sediment with a Cr/Ti ratio of 1.87×10^{-2}, consistent with typical values from pelagic red clays (53–55), accumulating at a burial rate of 1.0×10^{-3} $g \cdot cm^{-2} \cdot y^{-1}$. Because the burial of Cr in oxic settings should depend on the efficiency of metal oxide burial, this burial rate is then combined with the same areal extent of oxic seafloor (defined by sediment O_2 penetration depth) discussed above.

The anoxic sink for Cr is defined in a similar manner to the sulfidic sink for Mo, a natural result of the fact that on the modern Earth the relative mobility and transport of S and Fe are such that anoxic settings tend to become euxinic (anoxic and sulfidic). We use Cr/Ti ratios from the Cariaco Basin (34, 56, 57) to obtain a modern anoxic burial rate of ~0.5 $\mu g \cdot cm^{-2} \cdot y^{-1}$, and scale this to the seafloor area of anoxic environments as discussed above for the modern Mo budget. This burial rate is roughly of the same order as that for Mo in euxinic settings, although we acknowledge that these estimates will improve with further generation and analysis of Cr data in anoxic marine systems. However, Cr will be reduced and immobilized as Cr(III) via a wide range of reductants—dissolved H_2S is not necessary (58–60). Indeed, Cr(VI) reduction to Cr(III) has been shown to take place in the open-water column of the eastern tropical Pacific, coincident with the onset of microbial denitrification (61). This provides a crucial distinction with the behavior of Mo, in that effective Mo capture requires the additional presence of free dissolved sulfide, and forms the centerpiece of our analysis. The reducing sediment sink is again solved for using the other parameters of the budget. We assume an authigenic burial rate of 0.15 $\mu g \cdot cm^{-2} \cdot y^{-1}$, derived from combining Cr/Ti ratios in the Gulf of California (62) with the requisite bulk MAR (63). This aspect of the budget is not well constrained, but we consider it unlikely that such settings will authigenically bury Cr at rates much higher than this. In other words, we use what we consider to be a relatively high burial rate to avoid underestimating the magnitude of this sink relative to the anoxic sink, rendering this portion of the budget conservative for the conclusions presented here. Parameters for our modern balanced Cr budget are shown in Fig. S2 and Table S4.

Hydrothermal Cycling of Mo and Cr. The systematics of Mo and Cr in hydrothermal systems and the effects of hydrothermal processes on the Earth surface cycles of Mo and Cr have not been explored in detail, but we can place some basic constraints on the possible effects of high- and low-temperature seawater–basalt interaction on the mass balances of Mo and Cr in the ocean. The water flux through a high-temperature hydrothermal system ($F_{(ht)}$; in $kg \cdot y^{-1}$) can be estimated as (64)

$$F_{(ht)} = \frac{Q_{(ht)}}{\Delta T_{(ht)} c_p},$$

where $Q_{(ht)}$ is the hydrothermal heat flux, $\Delta T_{(ht)}$ is the seawater temperature anomaly, and c_p is the specific heat of seawater (at

seafloor pressure and vent fluid temperature). We can combine this with a concentration anomaly for a given metal ($\Delta[Me] = [Me]_{SW} - [Me]_{fluid}$) to estimate a high-temperature hydrothermal flux to/from seawater (F_{hyd}) as

$$F_{(ht)} = \frac{Q_{(ht)}}{\Delta T_{(ht)} c_p} \Delta[\mathrm{Me}],$$

Results of this calculation for both Mo and Cr are shown in Table S5. These calculations suggest that high-temperature seawater–basalt interaction represents a removal flux of both Mo and Cr that is very small relative to the riverine flux of either element. We note that such estimates are inherently imprecise, given uncertainties in the magnitude of on-axis heat flow (ref. 64 and references therein) and analytical difficulties associated with obtaining unadulterated fluid chemistry. In the case of high-temperature fluids, it is most likely that these concentrations have been perturbed by mixing with seawater Cr and/or Mo, which would cause us to underestimate the magnitude of these sink terms. However, this should have a negligible effect on our result, given that reported concentration anomalies indicate near-complete removal of both elements during high-temperature seawater–basalt interaction (Table S5). Assuming complete removal of seawater Mo from the circulating fluid (i.e., $\Delta[Mo] = 107$ nM) would increase our estimated high-temperature removal flux from 0.85 to 0.91% of the total input flux. Making the same assumption for Cr (i.e., $\Delta[Cr] = 4$ nM), would have a trivial effect on the estimated high-temperature removal flux.

Low-temperature, off-axis hydrothermal systems are a much more difficult problem to address. Pristine vent fluid composition is not well constrained for many settings, but, more importantly, the global water flux through such systems is very poorly constrained. Given that the temperature anomaly is probably small, a much larger water flux would be necessary to dissipate the requisite heat flow. As a result, even a very small concentration anomaly may result in a significant flux to/from seawater on a global scale. Magnesium (Mg^{2+}) substitutes readily for calcium (Ca^{2+}) during seafloor basalt alteration (65), and is removed from seawater during hydrothermal fluid evolution at both high and low temperature (66–68). Using the above method of calculation, the high-temperature removal flux of Mg^{2+} from seawater can be estimated as $\sim 1.3 \times 10^{12}$ mol·y^{-1}. By combining the global discharge rate used above with a global average riverine Mg^{2+} concentration of 128 μmol·kg^{-1} (69), we derive a global riverine Mg^{2+} flux of $\sim 5.0 \times 10^{12}$ mol·y^{-1}. If we assume that the balance between the riverine flux and removal during high-temperature seawater–basalt interaction is made up by low-temperature flow, we can use the Mg^{2+} concentration anomaly ($\Delta[Mg^{2+}] = [Mg^{2+}]_{SW} - [Mg^{2+}]_{fluid}$) of well-constrained diffuse flow systems such as that along the Juan de Fuca Ridge to calculate an approximate water flux through such systems of 9.5×10^{13} kg·y^{-1}.

Combining this estimated water flux with available chemical anomalies for Mo and Cr allows us to place rough limits on the magnitude of the low-temperature fluxes of these elements to seawater (Table S6). These may be upper limits given available constraints, as the calculations assume no other removal fluxes of Mg^{2+} from seawater [i.e., uptake during carbonate burial or clay mineral alteration during "reverse weathering" reactions (70)]. We suggest that although low-temperature fluxes are likely to be somewhat larger than those that occur during on-axis fluid flow, they are still a relatively small fraction of the corresponding riverine fluxes. Given the framework outlined above, it is highly unlikely that the flux of either element will exceed ~10% of their respective riverine inputs. Furthermore, as stated above, sensitivity analysis indicates that our results are not strongly affected by reasonable changes in Cr and/or Mo input fluxes (Fig. S2).

Offshore Scaling of Metal Burial Rates in the Model. Our modeling approach essentially involves balancing the modern steady-state cycles of both Cr and Mo and applying a continuous range of perturbations to this balanced cycle to explore the new steady state attained under different oceanic redox regimes. In doing so, we begin with a conventional first-order mass balance formulation. This class of model, often used to explore the dynamics of various chemical tracers in the ocean and their isotope systems, makes the implicit assumption that the burial fluxes characteristic of some particular environment (typically organic-rich continental margin sediments or marginal restricted basins) can be universally applied to extremely large regions of the seafloor. In other words, it is assumed that a burial rate characteristic of, say, the Peru margin can be applied to the abyssal realm of the ocean. This is almost certainly physically unrealistic, as open ocean settings are characterized by much lower bulk sediment fluxes, and, in particular, organic carbon fluxes (71–74). As a result, if a particular region of the abyssal ocean becomes authigenically active for some chemical constituent of seawater, it can be expected that the removal rates of that constituent into the sediment column will be much lower than those seen in more marginal settings. The net result will be a system that is overly sensitive to perturbation, as burial fluxes in large regions of the deep sea will be overestimated. This dilemma, inherent in conventional first-order mass balance analysis, has been noted by some previous work (75, 76) but has not been explored in detail. This problem is particularly acute for redox-sensitive transition metals, such as Mo and Cr, given that the organic matter flux is typically thought to be directly involved in metal sequestration (e.g., ref. 36).

We have attempted to alleviate this problem by adding a "pseudospatial" dimension to the conventional one-box ocean mass balance approach. We take an algorithm used in global diagenetic models (77) for organic carbon flux to the seafloor as a function of depth, which is then coupled to a polynomial function fitted to bathymetric data for the modern ocean (78). We then use a burial flux ratio ($R_{Me/C}$, where Me refers to Mo or Cr) for each element, a tuned parameter resulting in a relationship that encodes a decrease in local (and globally averaged) metal burial rates as larger regions of the seafloor become authigenically active. Values for $R_{Me/C}$ are tuned to reproduce the modern condition (i.e., the modern globally averaged burial rates at ~0.1% seafloor anoxia; Fig. S4). The essential concept here is that a given region of the seafloor has a characteristic burial capacity for either Cr or Mo, regulated to first order by the relative carbon flux through the water column and to the sediments, and that this burial capacity will only be reached when a region of the ocean achieves the requisite redox characteristics for each metal.

We stress that because the metal burial rates are derived by using a tunable ratio, this pattern is not explicitly dependent on the absolute value of the carbon flux to the seafloor at a given depth—rather, it hinges on the observation that carbon fluxes to the seafloor will decrease as one moves out into the deep sea, with the first-order topology depicted in Fig. S3. This is important, as dramatically different redox structures within the ocean, extreme differences in the composition of primary producing communities, mineral ballasting, etc., might be expected to result in significant differences in the absolute value of the carbon flux to the seafloor within different regions of the ocean. However, we consider it unlikely that the basic pattern of an offshore decrease in carbon fluxes has changed much throughout Earth's history on a global scale. In addition, although the basic bathymetry of the ocean has doubtless changed throughout Earth's history, we consider the modern depth–area curve to represent a reasonable first approximation. This approach must ultimately be refined if used in efforts to delineate more subtle changes in ocean redox, or if applied to periods during which continental

configuration and/or bathymetry are better constrained, but we contend that it provides a much more realistic depiction of the sensitivity of Cr and Mo mass balance to perturbation than previous model treatments. Further work should focus on the development and implementation of more spatially explicit approaches for dealing with the effects of seafloor redox perturbation on biogeochemical cycling and isotope systematics, for example coupling efficient models of benthic diagenesis that can be forced by gridded domains (79) to Earth system models of intermediate complexity (e.g., GENIE; ref. 80).

Prescribed Perturbations in the Model and the Role of Reducing Sediments. As discussed above, our model analysis involves balancing the modern steady-state cycles of Cr and Mo, applying a continuous range of perturbations to seafloor redox state, and establishing the ultimate steady-state conditions and local burial rates attained by the model system. Because our model includes a representation of offshore decreases in authigenic burial rates, essentially a spatial component, we must make some explicit assumptions about the basic seafloor environments in which perturbations begin and expand.

We assume first that ~5% of the shallow seafloor remains essentially authigenically neutral unless it becomes absolutely necessary to encroach upon this area (i.e., above 95% seafloor anoxia or euxinia). This assumption is meant to encompass coastal sediments deposited within the well-oxygenated mixed layer of the ocean. In addition, we assume that if atmospheric oxygen levels are low enough such that large portions of the oceanic mixed layer are anoxic, then the vast majority of the ocean will almost certainly be anoxic as well, effectively rendering the exercise moot and making our conclusions with respect to anoxia rather self-evident without changing our conclusions with respect to euxinia. Perturbations are then applied by expanding a given redox state (anoxic or euxinic) from the shallow shelf out into the deep sea. An important corollary of this approach is that during a given perturbation the first environments to become authigenically active are characterized by the highest metal burial rates. We view this as generally justifiable on mechanistic grounds, as elevated carbon fluxes through the water column and water column oxidant depletion are most commonly seen along ocean margins.

However, it is important to entertain the possibility that the nature of perturbations to seafloor redox may not be the same for Cr and Mo. For example, given that deep-sea anoxia during the mid-Proterozoic was most likely caused by gas-exchange constraints expressed in deep-water formation regions (81), rather than local reductant (i.e., carbon) input, it may be argued that large regions of the deep sea would first become anoxic and authigenically active for Cr, whereas euxinic environments driven by the combined effects of more reducing source waters and local carbon flux would be limited to marginal environments. In effect, this would result in less efficient Cr removal and similar Mo removal compared with the results presented here, which would in turn require a larger area of marine anoxia for a given Cr reservoir change. Thus, to remain conservative we prescribe that perturbations to both models begin and expand from settings where metal accumulation rates are highest. The reverse scenario, in which euxinia develops first in the abyssal realm of the ocean but anoxia is confined to the shelves, is difficult to imagine simply because of regional variability in carbon flux.

Another important assumption that is made in our modeling exercise is that the seafloor area of reducing sediments is fixed at a constant value (~1.9% for the Mo model and ~4.9% for the Cr model). However, it is reasonable to expect that if the ocean becomes less oxygenated on a global scale there should be a first-order expansion of reducing sediment environments. With respect to our basic conclusions, it is clear that this is a much larger concern for Cr than for Mo. Expanding the reducing sediment sink in the Mo model would only serve to decrease the extent of euxinic seafloor inferred for a given calculated enrichment. In other words, our interpretation that the mid-Proterozoic Mo enrichment record in euxinic shales implies relatively limited euxinic seafloor is rendered conservative by neglecting the expansion of reducing sediments in the model, and our conclusion that euxinia represents a small relative fraction of overall anoxia will remain unchanged. In the case of Cr, it might be argued that expansion of the reducing sediment sink together with expanding anoxia could result in our model significantly overestimating the amount of anoxic seafloor necessary to drive shifts in the seawater Cr reservoir. We consider this a problem that is somewhat scale-dependent, and that it is unlikely to change our fundamental conclusions for two reasons. First, in our model experiments we have artificially enhanced the impact of the reducing sediment sink, by choosing a relatively high Cr burial rate and by specifying that this burial rate applies to ~5% of the seafloor in addition to the expansion of anoxia in shelf environments. When we consider that the offshore scaling of metal burial rates (Fig. S4) should equally well apply to reducing sediment environments, this essentially amounts to "double counting" ~5% of the seafloor as being both reducing sediments and anoxic, with the highest metal burial rates specified for both. Alternatively, we can envision this as representing the exclusive expansion of anoxia in marginal settings, whereas ~5% of the seafloor offshore is covered by reducing sediments with unrealistically high burial rates. In either case, alternative approaches would need to either expand the reducing sediment sink at the expense of anoxic environments on the shelf, or expand it within the deep sea where metal burial capacity decreases sharply (Fig. S4). Both approaches would yield a comparable (and in some cases smaller) overall removal flux into reducing sediment environments.

Lastly, it is unlikely for very large regions of the seafloor to be characterized by this type of chemical environment at steady-state timescales. Such systems can be driven by sharp redox gradients, as often occurs in modern continental margin settings, but these environments require a rather unique combination of extremely high organic matter (i.e., reductant) loading and a degree of bottom-water ventilation such that the system does not become truly anoxic. Such sharp redox gradients will be difficult to maintain across large regions of the deep sea as a result of generally attenuated local organic carbon flux to offshore sediments. Alternatively, such a system can be driven by oxidant limitation. However, it is difficult to imagine this kind of system persisting on an extremely large scale, as it is poorly redox-buffered—small changes to circulation or carbon flux will result in the development of either true anoxia or increased bottom water O_2 such that the environment becomes effectively oxic with respect to metal burial.

Using the Model to Calculate Authigenic Metal Enrichments. From a qualitative perspective, it is difficult to avoid the conclusion that the coupled enrichment records require much more pervasive anoxia than that implied by equivalent Phanerozoic settings, but also that the relative fraction of anoxia represented by sulfidic deposition was not large. Our attempt to place more quantitative constraints on this conceptual interpretation involves using the scaling between seawater reservoir size and metal burial rates (inherent in a first-order mass balance model) to estimate sedimentary enrichments by assuming a bulk MAR in a hypothetical siliciclastic-dominated continental margin setting.

These two parameters (authigenic metal burial rate and bulk sediment MAR) should not be arbitrarily decoupled. This is true arithmetically, as metal burial rates in modern settings are in fact derived from bulk MARs. It is also expected on mechanistic grounds, as higher bulk MARs result in more rapid delivery of reactive mineral surfaces and organic carbon, and more rapid and efficient burial of authigenically sequestered elements. Indeed, there is good evidence from a range of modern (82) and ancient (83) settings that metal burial rates will scale in a general sense

with bulk sediment MARs—in other words, metal enrichments will not simply scale linearly with changes in MAR. This issue is similar to that discussed above, in that an arbitrary decoupling of metal burial rates from bulk MARs is akin to applying a metal burial rate from a continental margin setting to the abyssal realm of the ocean, an approach we consider physically unrealistic.

Because this scaling between metal burial rate and bulk MAR is a somewhat broad relationship, we use well-constrained recent Cariaco Basin sediment data as a guide. We separate the range of Cr and Mo burial rates and bulk MAR values constrained for the Cariaco Basin over the last ~20,000 y, and sequentially combine them to explore the effect of a reasonable decoupling between these two parameters (Fig. S5). In an effort to render our estimates conservative, we choose combinations of metal burial rate and bulk MAR that result in relatively low enrichments for Cr and relatively high enrichments for Mo, and these are presented in the main text (Fig. S5).

No single combination of parameters will be adequate to describe the entire shale record, but we view this broad range as sufficient to encompass the vast majority of environments represented in our database. It is apparent from this exercise that a very strong decoupling between metal burial rate and bulk MAR values, which we consider unrealistic, is necessary to invalidate our basic conclusions. Furthermore, this condition would need to pertain to every mid-Proterozoic anoxic shale in our database over ~1.5 Ga, whereas fortuitously being alleviated during the early Phanerozoic, a combination of circumstances that that would be improbable.

1. Lyons TW, Severmann S (2006) A critical look at iron paleoredox proxies: New insights from modern euxinic marine basins. *Geochim Cosmochim Acta* 70:5698–5722.
2. Poulton SW, Fralick PW, Canfield DE (2004) The transition to a sulphidic ocean approximately 1.84 billion years ago. *Nature* 431(7005):173–177.
3. Poulton SW, Canfield DE (2005) Development of a sequential extraction procedure for iron: implications for iron partitioning in continentally derived particulates. *Chem Geol* 214:209–221.
4. Poulton SW, Canfield DE (2011) Ferruginous conditions: A dominant feature of the ocean through Earth's history. *Elements* 7:107–112.
5. Canfield DE (1989) Reactive iron in marine sediments. *Geochim Cosmochim Acta* 53: 619–632.
6. März C, et al. (2008) Redox sensitivity of P cycling during marine black shale formation: Dynamics of sulfidic and anoxic, non-sulfidic bottom waters. *Geochim Cosmochim Acta* 72:3703–3717.
7. Lyons TW, et al. (2009) Tracking euxinia in the ancient ocean: A multiproxy perspective and Proterozoic case study. *Ann Rev Earth Planet Sci Lett* 37:507–534.
8. Raiswell R, Buckley R, Berner RA, Anderson TF (1988) Degree of pyritization of iron as a paleoenvironmental indicator of bottom-water oxygenation. *J Sed Petr* 58:812–819.
9. Algeo TJ, Maynard JB (2008) Trace-metal covariation as a guide to water-mass conditions in ancient anoxic marine environments. *Geosphere* 4:872–887.
10. Kump LR, et al. (2011) Isotopic evidence for massive oxidation of organic matter following the great oxidation event. *Science* 334(6063):1694–1696.
11. Planavsky NJ, Bekker A, Hofmann A, Owens JD, Lyons TW (2012) Sulfur record of rising and falling marine oxygen and sulfate levels during the Lomagundi event. *Proc Natl Acad Sci USA* 109(45):18300–18305.
12. Scott C, et al. (2008) Tracing the stepwise oxygenation of the Proterozoic ocean. *Nature* 452(7186):456–459.
13. Miller CA, Peucker-Ehrenbrink B, Walker BD, Marcantonio F (2011) Re-assessing the surface cycling of molybdenum and rhenium. *Geochim Cosmochim Acta* 75:7146–7179.
14. D'Hondt S, et al. (2009) Subseafloor sedimentary life in the South Pacific Gyre. *Proc Natl Acad Sci USA* 106(28):11651–11656.
15. Fischer JP, Ferdelman TG, D'Hondt S, Røy H, Wenzhöfer F (2009) Oxygen penetration deep into the sediment of the South Pacific gyre. *Biogeosciences* 6:1467–1478.
16. Froelich PN, et al. (1979) Early oxidation of organic matter in pelagic sediments of the eastern equatorial Atlantic: Suboxic diagenesis. *Geochim Cosmochim Acta* 43: 1075–1090.
17. Finney BP, Lyle MW, Heath GR (1988) Sedimentation at MANOP Site H (Eastern Equatorial Pacific) over the past 400,000 years: Climatically induced redox variations and their effects on transition metal cycling. *Paleoceanography* 3:169–189.
18. Burdige DJ (1993) The biogeochemistry of manganese and iron reduction in marine sediments. *Earth Sci Rev* 35:249–284.
19. Morford JL, Emerson S (1999) The geochemistry of redox sensitive trace metals in sediments. *Geochim Cosmochim Acta* 63:1735–1750.
20. Meile C, Van Cappellen P (2003) Global estimates of enhanced solute transport in marine sediments. *Limnol Oceanogr* 48:777–786.
21. Thullner M, Dale AW, Regnier P (2009) Global-scale quantification of mineralization pathways in marine sediments: A reaction-transport modeling approach. *Geochem Geophys Geosyst*, 10.1029/2009GC002484.
22. Bertine KK, Turekian KK (1973) Molybdenum in marine deposits. *Geochim Cosmochim Acta* 37:1415–1434.
23. Bender ML, Ku T-L, Broecker WS (1970) Accumulation rates of manganese in pelagic sediments and nodules. *Earth Planet Sci Lett* 8:143–148.
24. Shimmield GB, Price NB (1986) The behaviour of molybdenum and manganese during early sediment diagenesis – offshore Baja California, Mexico. *Mar Chem* 19:261–280.
25. Brüchert V, et al. (2003) Regulation of bacterial sulfate reduction and hydrogen sulfide fluxes in the central Namibian coastal upwelling zone. *Geochim Cosmochim Acta* 67:4505–4518.
26. Brüchert V, Currie B, Peard KR (2009) Hydrogen sulphide and methane emissions on the central Namibian shelf. *Prog Oceanogr* 83:169–179.
27. Piper DZ, Dean WE (2002) Trace element deposition in the Cariaco Basin, Venezuela shelf, under sulfate-reducing conditions - a history of the local hydrography and global climate, 20 ka to the present, USGS Professional Paper, Vol 1670, 45 pp.
28. Francois R (1988) A study on the regulation of the concentrations of some trace metals (Rb, Sr, Zn, Pb, Cu, V, Cr, Ni, Mn and Mo) in Saanich Inlet sediments, British Columbia, Canada. *Mar Geol* 83:285–308.
29. Ravizza G, Turekian KK, Hay BJ (1991) The geochemistry of rhenium and osmium in recent sediments from the Black Sea. *Geochim Cosmochim Acta* 55:3741–3752.
30. Algeo TJ (2004) Can marine anoxic events draw down the trace element inventory of seawater? *Geology* 32(12):1057–1060.
31. Buesseler KO, Benitez CR (1994) Determination of mass accumulation rates and sediment radionuclide inventories in the deep Black Sea. *Deep Sea Res Part I Oceanogr Res Pap* 41:1605–1615.
32. Dean WE, Piper DZ, Peterson LC (1999) Molybdenum accumulation in Cariaco basin sediment over the past 24 k.y.: A record of water-column anoxia and climate. *Geology* 27:507–510.
33. Giraudeau J, Meyers PA, Christensen BA (2002) Accumulation of organic and inorganic carbon in Pliocene-Pleistocene sediments along the SW African margin. *Mar Geol* 180: 49–69.
34. Lyons TW, Werne JP, Hollander DJ, Murray RW (2003) Contrasting sulfur geochemistry and Fe/Al and Mo/Al ratios across the last oxic-to-anoxic transition in the Cariaco Basin, Venezuela. *Chem Geol* 195:131–157.
35. Borchers SL, Schnetger B, Böning P, Brumsack H-J (2005) Geochemical signatures of the Namibian diatom belt: Perennial upwelling and intermittent anoxia. *Geochem Geophys Geosyst*, 10.1029/2004GC000886.
36. Algeo TJ, Lyons TW (2006) Mo-total organic carbon covariation in modern anoxic marine environments: Implications for analysis of paleoredox and paleohydrographic conditions. *Paleoceanography*, 10.1029/2004PA001112.
37. McManus J, et al. (2006) Molybdenum and uranium geochemistry in continental margin sediments: Paleoproxy potential. *Geochim Cosmochim Acta* 70:4643–4662.
38. Sifeddine A, et al. (2008) Laminated sediments from the central Peruvian continental slope: A 500 year record of upwelling system productivity, terrestrial runoff and redox conditions. *Prog Oceanogr* 79:190–197.
39. Gutierrez D, et al. (2009) Rapid reorganization in ocean biogeochemistry off Peru towards the end of the Little Ice Age. *Biogeosciences* 6:835–848.
40. Poulson Brucker RL, McManus J, Severmann S, Berelson WM (2009) Molybdenum behavior during early diagenesis: Insights from Mo isotopes. *Geochem Geophys Geosyst*, 10.1029/2008GC002180.
41. Brumsack H-J (1989) Geochemistry of recent TOC-rich sediments from the Gulf of California and the Black Sea. *Geol Rundsch* 78:851–882.
42. Zheng Y, Anderson RF, van Geen A, Kuwabara J (2000) Authigenic molybdenum formation in marine sediments: A link to pore water sulfide in the Santa Barbara Basin. *Geochim Cosmochim Acta* 64:4165–4178.
43. Poulson RL, Siebert C, McManus J, Berelson WM (2006) Authigenic molybdenum isotope signatures in marine sediments. *Geology* 34:617–620.
44. Peuker-Ehrenbrink B (2009) Land2Sea database of river drainage basin sizes, annual water discharges, and suspended sediment fluxes. *Geochem Geophys Geosyst*, 10.1029/2008GC002356.
45. Cranston RE, Murray JW (1980) Chromium species in the Columbia River and estuary. *Limnol Oceanogr* 25:1104–1112.
46. Abu-Saba KE, Flegal AR (1995) Chromium in San Francisco Bay: Superposition of geochemical processes causes complex spatial distributions of redox species. *Mar Chem* 49:189–199.
47. Jeandel C, Minster JF (1987) Chromium behavior in the ocean: Global versus regional processes. *Global Biogeochem Cycles* 1:131–154.
48. van der Weijden CH, Reith M (1982) Chromium(III) – chromium(VI) interconversions in seawater. *Mar Chem* 11:565–572.
49. Ellis AS, Johnson TM, Bullen TD (2004) Using chromium stable isotope ratios to quantify Cr(VI) reduction: Lack of sorption effects. *Environ Sci Technol* 38(13): 3604–3607.
50. Smith E, Ghiassi K (2006) Chromate removal by an iron sorbent: Mechanism and modeling. *Water Environ Res* 78(1):84–93.
51. Zachara JM, Girvin DC, Schmidt RL, Resch CT (1987) Chromate adsorption on amorphous iron oxyhydroxide in the presence of major groundwater ions. *Environ Sci Technol* 21(6):589–594.
52. Zachara JM, Cowan CE, Schmidt RL, Ainsworth CC (1988) Chromate adsorption by kaolinite. *Clays Clay Miner* 36:317–326.
53. Turekian KK, Imbrie J (1966) The distribution of trace elements in deep-sea sediments of the Atlantic Ocean. *Earth Planet Sci Lett* 1:161–168.
54. Chester R, Hughes MJ (1969) The trace element geochemistry of a North Pacific pelagic clay core. *Deep-Sea Res* 16:639–654.

55. Cronan DS (1969) Average abundances of Mn, Fe, Ni, Co, Cu, Pb, Mo, V, Cr, Ti and P in Pacific pelagic clays. *Geochim Cosmochim Acta* 33:1562–1565.
56. Piper DZ, Dean WE (2002) Trace-element deposition in the Cariaco Basin under sulfate reducing conditions—a history of the local hydrography and global climate, 20 ka to present. USGS Professional Paper (US Geological Survey, Denver), Vol 1670, 41 pp.
57. Dean WE (2007) Sediment geochemical records of productivity and oxygen depletion along the margin of western North America during the past 60,000 years: Teleconnections with Greenland Ice and the Cariaco Basin. *Q Sci Rev* 26:98–114.
58. Eary LE, Rai D (1989) Kinetics of chromate reduction by ferrous ions derived from hematite and biotite at 25°C. *Am J Sci* 289:180–213.
59. Fendorf SE, Li G (1996) Kinetics of chromate reduction by ferrous iron. *Environ Sci Technol* 30:1614–1617.
60. Bond DL, Fendorf S (2003) Kinetics and structural constraints of chromate reduction by green rusts. *Environ Sci Technol* 37(12):2750–2757.
61. Rue EL, Smith GJ, Cutter GA, Bruland KW (1997) The response of trace element redox couples to suboxic conditions in the water column. *Deep Sea Res Part I Oceanogr Res Pap* 44:113–134.
62. Brumsack H-J, Gieskes JM (1983) Interstitial water trace-metal chemistry of laminated sediments from the Gulf of California, Mexico. *Mar Chem* 14:89–106.
63. Calvert SE (1966) Accumulation of diatomaceous silica in sediments of the Gulf of California. *Bull Geol Soc Amer* 77:569–596.
64. Elderfield H, Schultz A (1996) Mid-ocean ridge hydrothermal fluxes and the chemical composition of the ocean. *Annu Rev Earth Planet Sci* 24:191–224.
65. Berner RA (2004) A model for calcium, magnesium and sulfate in seawater over Phanerozoic time. *Am J Sci* 304:438–453.
66. Seyfried WE, Jr., Mottle MJ (1982) Hydrothermal alteration of basalt by seawater under seawater-dominated conditions. *Geochim Cosmochim Acta* 46:985–1002.
67. Von Damm KL, Edmond JM, Measures CI, Grant B (1985) Chemistry of submarine hydrothermal solutions at Guymas Basin, Gulf of California. *Geochim Cosmochim Acta* 49:2221–2237.
68. Wheat CG, Mottl MJ, Rudnicki M (2002) Trace element and REE composition of a low-temperature ridge-flank hydrothermal spring. *Geochim Cosmochim Acta* 66: 3693–3705.
69. Emerson S, Hedges J (2008) *Chemical Oceanography and the Marine Carbon Cycle* (Cambridge Univ Press, Cambridge, UK).
70. Michalopoulos P, Aller RC (1995) Rapid clay mineral formation in Amazon Delta sediments: Reverse weathering and oceanic elemental cycles. *Science* 270:614–617.
71. Jahnke RA (1996) The global ocean flux of particulate organic carbon: Areal distribution and magnitude. *Global Biogeochem Cycles* 10:71–88.
72. Middelburg JJ, Soetaert K, Herman PMJ (1997) Empirical relationships for use in global diagenetic models. *Deep Sea Res Part I Oceanogr Res Pap* 44:327–344.
73. Sarmiento JL, Gruber N (2006) *Ocean Biogeochemical Dynamics* (Princeton Univ Press, Princeton).
74. Dunne JP, Sarmiento JL, Gnanadesikan A (2007) A synthesis of global particle export from the surface ocean and cycling through the ocean interior and on the seafloor. *Global Biogeochem Cycles* 21:10.1029/2006GB002907.
75. Dahl TW, et al. (2010) Devonian rise in atmospheric oxygen correlated to the radiations of terrestrial plants and large predatory fish. *Proc Natl Acad Sci USA* 107(42):17911–17915.
76. Dahl TW, et al. (2011) Molybdenum evidence for expansive sulfidic water masses in ~750 Ma oceans. *Earth Planet Sci Lett* 311:264–274.
77. Middelburg JJ, Soetaert K, Herman PMJ, Heip CHR (1996) Denitrification in marine sediments: A model study. *Global Biogeochem Cycles* 10:661–673.
78. Menard HW, Smith SM (1966) Hypsometry of ocean basin provinces. *J Geophys Res* 71: 4305–4325.
79. Archer DE, Morford JL, Emerson SR (2002) A model of suboxic sedimentary diagenesis suitable for automatic tuning and gridded global domains. *Global Biogeochem Cycles* 16:10.1029/2000GB001288.
80. Ridgwell A, et al. (2007) Marine geochemical data assimilation in an efficient Earth System Model of global biogeochemical cycling. *Biogeosciences* 4:87–104.
81. Canfield DE (1998) A new model for Proterozoic ocean chemistry. *Nature* 396: 450–453.
82. Meyers SR, Sageman BB, Lyons TW (2005) Organic carbon burial rate and the molybdenum proxy: Theoretical framework and application to Cenomanian-Turonian oceanic anoxic event 2. *Paleoceanography* 20:10.1029/2004PA001068.
83. Hetzel A, Böttcher ME, Wortmann UG, Brumsack H-J (2009) Paleo-redox conditions during OAE 2 reflected in Demerara Rise sediment geochemistry (ODP Leg 207). *Palaeogeogr Palaeoclimatol Palaeoecol* 273:302–328.

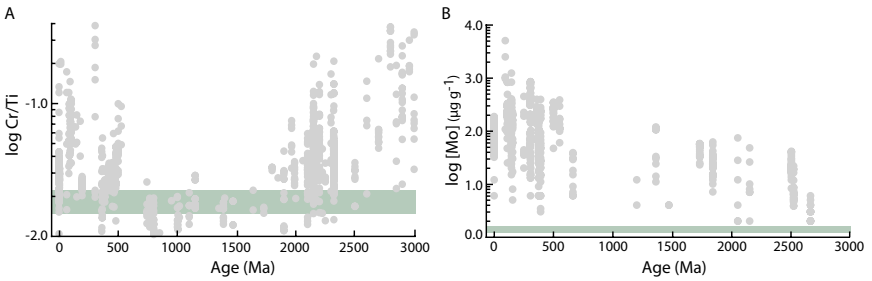

Fig. S1. Complete database for Cr (*A*) and Mo (*B*) enrichments through time, filtered according to protocols discussed in the text. Shaded boxes denote the range of upper modern crustal concentrations.

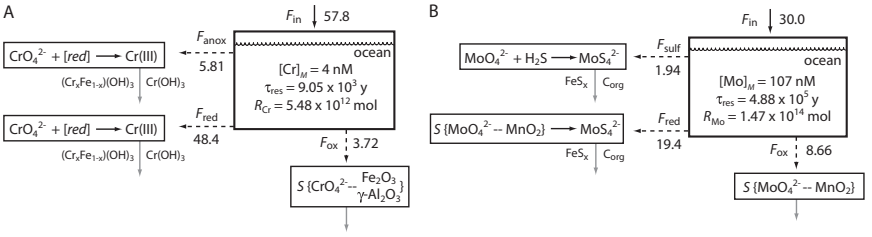

Fig. S2. Schematic of the global Cr (*A*) and Mo (*B*) mass balance models, showing the modern balanced state. Average modern seawater concentrations ($[Cr]_M$ and $[Mo]_M$), reservoir sizes (R_{Cr} and R_{Mo}), and residence times (τ_{res}) are shown. Dominant authigenic removal processes are depicted schematically for each sink [oxic (*ox*), anoxic (*anox*), reducing (*red*), and sulfidic (*sulf*) sinks]. C_{org} represents organic carbon, whereas terms shown as *S*{*x*–*y*} denote sorption processes. Hydrothermal fluxes are neglected in our treatment here (see *SI Discussion* for further details). Fluxes are in 10^7 mol·y^{-1}.

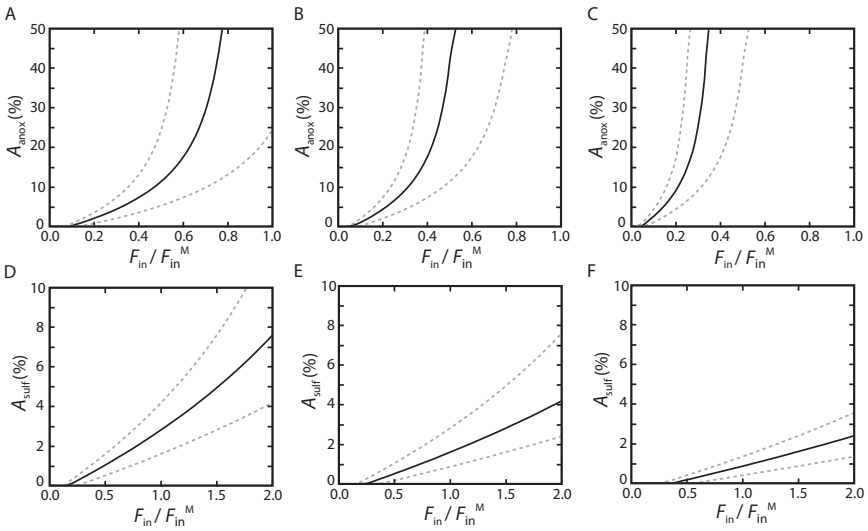

Fig. S3. Effect of changes in the assumed input flux on model results. *A–C* apply to the Cr model. Each curve shows the areal extent of seafloor anoxia (A_{anox}) at which authigenic Cr enrichments decrease below 5 $\mu g \cdot g^{-1}$. Each panel represents a different bulk MAR (increasing from left to right, with a range of a factor of 1.5 around 1.0×10^{-2} $g \cdot cm^{-2} \cdot y^{-1}$, the approximate value for deep sediments of the modern Cariaco Basin), whereas the curves represent low (dashed gray; 0.5 $\mu g \cdot cm^{-2} \cdot y^{-1}$), medium (black; 0.75 $\mu g \cdot cm^{-2} \cdot y^{-1}$) and high (dashed gray; 1.0 $\mu g \cdot cm^{-2} \cdot y^{-1}$) authigenic Cr burial rates. *D–F* apply to the Mo model, with each curve showing the areal extent of sulfidic (euxinic) seafloor (A_{sulf}) at which authigenic Cr enrichments decrease below 40 $\mu g \cdot g^{-1}$ (the mid-Proterozoic total mean). The range of bulk MAR values is the same as in *A–C*, with the various curves in each panel representing low (dashed gray; 1.0 $\mu g \cdot cm^{-2} \cdot y^{-1}$), medium (black; 1.5 $\mu g \cdot cm^{-2} \cdot y^{-1}$), and high (dashed gray; 2.0 $\mu g \cdot cm^{-2} \cdot y^{-1}$) authigenic Mo burial rates.

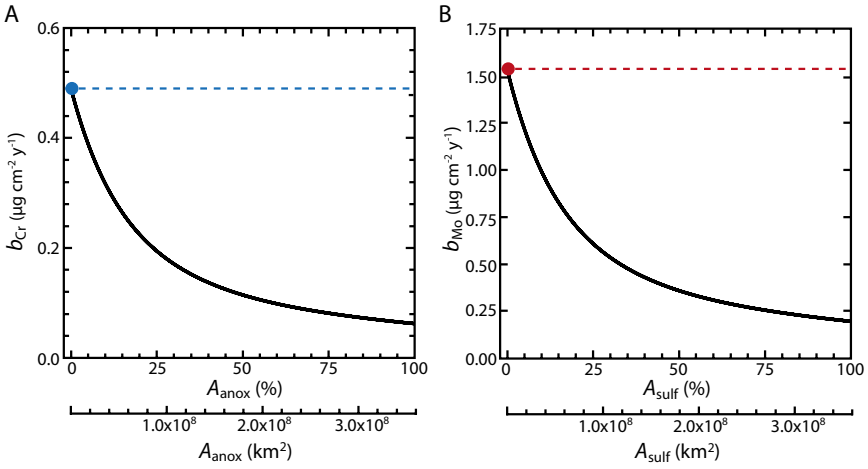

Fig. S4. Parametrization of offshore metal burial rate scaling in the model. Globally averaged authigenic Cr burial rates are shown in *A* as a function of anoxic seafloor area (A_{anox}). The blue filled circle represents the modern state, with the blue dotted line depicting a constant burial rate decoupled from the extent of anoxic seafloor area. Globally averaged authigenic Mo burial rates are shown in *B* as a function of sulfidic (euxinic) seafloor area (A_{sulf}). The red filled circle represents the modern state, with the red dotted line depicting a constant burial rate decoupled from the extent of euxinic seafloor area (essentially the models used in refs. 1–4).

1. Scott C, et al. (2008) Tracing the stepwise oxygenation of the Proterozoic ocean. *Nature* 452(7186):456–459.
2. Dahl TW, et al. (2010) Devonian rise in atmospheric oxygen correlated to the radiations of terrestrial plants and large predatory fish. *Proc Natl Acad Sci USA* 107(42):17911–17915.
3. Dahl TW, et al. (2011) Molybdenum evidence for expansive sulfidic water masses in ~750 Ma oceans. *Earth Planet Sci Lett* 311:264–274.
4. Kendall B, Creaser RA, Gordon GW, Anbar AD (2009) Re-Os and Mo isotope systematics of black shales from the Middle Proterozoic Velkerri and Wollogorang Formations, McArthur Basin, northern Australia. *Geochim Cosmochim Acta* 73:2534–2558.

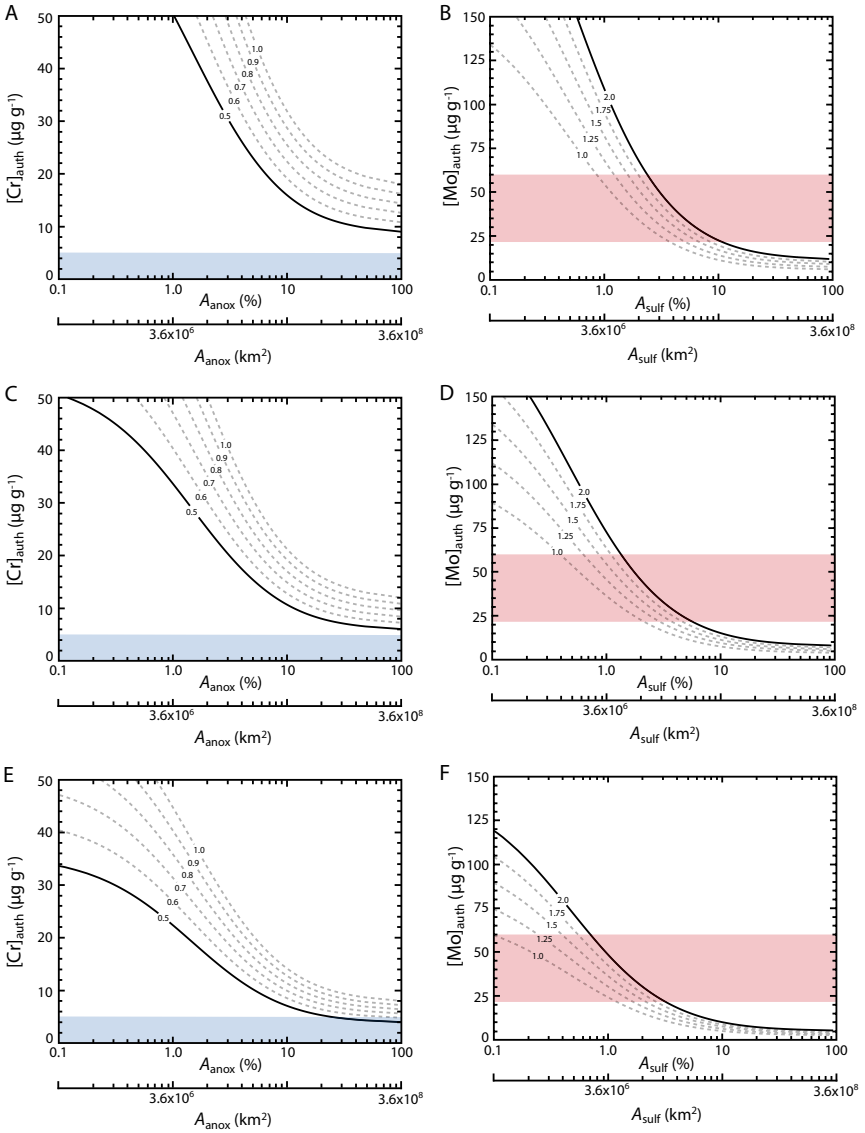

Fig. S5. Range of metal burial rates and bulk sediment MAR explored in the model. *A*, *C*, and *E* depict estimated authigenic Cr enrichments as a function of anoxic seafloor area at a range of plausible metal burial rates and bulk sediment MAR. The blue box represents our conservative threshold for Cr enrichment as constrained by the shale record. *B*, *D*, and *F* depict estimated authigenic Mo enrichments as a function of sulfidic (euxinic) seafloor area at a range of plausible metal burial rates and bulk sediment MAR. The red box represents the 95% confidence interval around the overall mean for the mid-Proterozoic shale enrichment record. Each panel represents a different bulk MAR (increasing from top to bottom, and depicting a range of a factor of 1.5 around 1.0×10^{-2} g·cm^{-2}·y^{-1}, the approximate value for deep sediments of the modern Cariaco Basin) and the contours are labeled by authigenic metal burial rate (in μg·cm^{-2}·y^{-1}). The solid black curves are those depicted in the main text.

Other Supporting Information Files

Table S1 (DOCX)
Table S2 (DOCX)
Table S3 (DOCX)
Table S4 (DOCX)
Table S5 (DOCX)
Table S6 (DOCX)